Laser Absorption Wave Formation

P. D. Thomas*

Lockheed Palo Alto Research Laboratory, Palo Alto, Calif.

The interaction region over an opaque solid target that is vaporizing under irradiation by an intense laser beam is modeled by a layer of expanding vapor and an air shock layer. It is shown that the formation of a subsonic laser-absorption wave in the air is triggered by laser-induced heating of the gas, and this heating occurs first in the vapor rather than in the shocked air. The role of nonequilibrium phenomena is reviewed, and a scaling law is given that determines the laser intensity-wavelength regime over which such phenomena can occur. A numerical solution of the interaction problem is developed that accounts for gasdynamics and radiative transport in the gas layers, and for heat conduction within the target. The computed results agree with experiments in which subsonic absorption waves have been observed to form over metal targets irradiated by a CO_2 gas laser at intensities of 0.1-1 Mw/cm^2. This agreement confirms the validity of the theoretical analysis as a useful tool for investigating the laser-target interaction and subsonic absorption wave formation phenomena for laser beam and target parameters other than those of the experiments.

I. Introduction

IT has been discovered experimentally that, when an opaque solid target is irradiated in the atmosphere by an intense laser beam under conditions where the ambient air normally would be transparent to the laser beam, the interaction between beam and target can lead to the formation of laser-absorption waves. These waves, which propagate up the laser beam through the ambient atmosphere toward the laser energy source, are narrow zones within which the air is hot, is highly ionized, and strongly absorbs the incident laser energy. Thus, the formation of a laser-absorption wave is connected with laser-induced heating of the gas layers near the target surface, and with the subsequent self-shielding of the target. We have postulated a simple model of the interaction that is predicated on uniform, bulk vaporization of the target surface, as opposed to nonuniform vaporization of localized surface sites, such as might occur in the neighborhood of surface imperfections.

The model (Fig. 1) consists of a thin surface zone within which the solid absorbs the incident energy and is converted into vapor, and a layer of vapor that expands away from the target surface. The moving vapor acts as a piston and drives a shock wave into the ambient air. Both the vapor and the shocked air may contain species that are capable of absorbing laser energy. Of fundamental interest are the continuous absorption mechanisms that are potentially important in either the vapor or air regardless of the composition of the vapor or of the wavelength. For the laser wavelength range of 1-10μ, the dominant mechanism of this type is the inverse bremsstrahlung absorption by free electrons.

II. Physics of the Gas Heating Process

Basic Phenomena

Inverse bremsstrahlung absorption of laser energy potentially can occur in both the target vapor and in the air that is disturbed by gasdynamic interaction with the vapor. To deter-

mine which of these regions is the more important, we have obtained estimates of the initial state of the gas that are valid prior to the time when significant heating of the gas takes place.[3] On the basis of these estimates, we have found that significant heating will take place first in the evolved vapor rather than in the shocked air layer.

For simple metallic targets (e.g., aluminum) that emit simple monatomic vapors, we assume that the vapor initially generated at the surface is in a state of local thermodynamic equilibrium (LTE), including phase equilibrium. The weakly ionized vapor contains a significant population of free electrons, even at the low laser fluxes (low vaporization rates) for which the surface pressure is only slightly above ambient. This is a result of the rather high vaporization temperature (2750 K at 1 atm) and low ionization potential (6 ev) of aluminum vapor. Thus, a significant vapor heating is to be expected as a result of inverse bremsstrahlung absorption of laser energy.

In contrast, the electron density in the shocked air is substantially below that in the vapor, partly because air has a much higher effective ionization potential, and partly because the shock-heating mechanism is inefficient. Very high laser fluxes (high vaporization rates) are required to shock-heat the air to temperatures where the electron density is comparable to that in the vapor.

A similar situation exists for most opaque materials; the vaporization temperatures are in the range 2500-4000 K and the ionization potentials of their vapor products are generally lower than that of air. The conditions in the shocked air layer as a function of laser flux absorbed at the target are very insensitive to the type of material or to its chemical com-
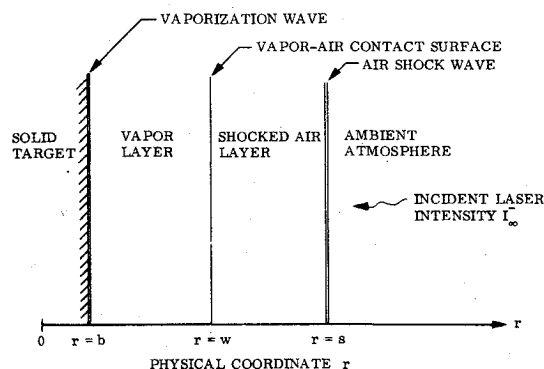

Fig. 1 Diagram of interaction region.

position.[4] As a consequence, laser energy absorption and heating will take place more readily in the vapor than in the shocked air.

The absorption coefficient is so low at pressures of the order of 1 atm and temperatures near the vaporization temperature that a very thick vapor layer would have to be built up to attenuate the incident energy significantly. If the heating rate exceeds the rate of cooling by gasdynamic expansion, the increase in the equilibrium degree of ionization that accompanies the rise in temperature will accelerate the onset of self-shielding. However, at very high laser fluxes, fast nonequilibrium processes arise that are similar to those responsible for laser-induced breakdown of cold air.[1,2] Breakdown occurs when the electrons acquire laser energy faster than they can cool by competing processes. Collisional ionization of atoms by these energetic electrons produces an electron avalanche in which the electron density grows exponentially in time, and the gas quickly becomes opaque to the laser beam.

Nonequilibrium Effects

We have determined the regimes of laser intensity, wavelength, target material, etc., where the described nonequilibrium processes affect the laser energy absorption by the gas. The role of nonequilibrium effects in the vapor has been assessed by comparing the kinetic rates of microscopic energy transfer processes.[3]

The principal nonequilibrium effect is avalanche ionization, which results from a lack of translational equilibrium between free electrons and heavy particles. The free electrons heat by inverse bremsstrahlung absorption of laser energy, and will be driven out of translational equilibrium with the heavy particles unless the heating rate is small compared to the rate of energy transfer from the electrons via elastic collisions with atoms. These competing processes can be characterized in terms of the electron heating time τ_I, defined as the time required for the electrons to heat to twice their intial average energy, and the relaxation time τ_{ea} for energy transfer in electron-atom elastic coolisions. The characteristic times are given by the equations

$$\tau_I^{-1} = \kappa_{ea} I / [\,(3/2)kT_e\, n_e]$$ (1a)

$$\tau_{ea}^{-1} = 2(m_e/m_a)\, n_a \Omega_{tr}$$ (1b)

$$\kappa_{ea} = e^2 n_e n_a \Omega_{tr} / \pi m_e c v^2$$ (1c)

where I is the laser intensity, k is Boltzmann's constant, T_e the electron temperature, n_e and n_a the electron and atom number densities, m_e and m_a the masses of electron and atom, κ_{ea} the electron-atom inverse bremsstrahlung absorption coefficient, e the electron charge, c the speed of light, and v the laser frequency; and the momentum transfer collision rate $\Omega_{tr} = \langle\sigma_{tr}\,V_e\rangle$ is the product of the momentum transfer cross section and electron velocity, averaged over a Maxwellian electron velocity distribution.

Equilibrium will be maintained during the heating process only if $\tau_I \ll \tau_{ea}$. Upon taking the ratio of the two characteristic times, we obtain a scaling law that determines the extent of the nonequilibrium regime. The resulting scaling law can be represented in terms of a "characteristic" laser intensity

$$I_c = 10^5 \,(10.6/\lambda)^2 \,(T_v/2750)\,(27/A)\,\text{w/cm}^2$$ (2)

that separates the equilibrium and nonequilibrium regimes for a target that vaporizes at temperature T_v and that emits a monatomic vapor of atomic weight A, where λ is the laser wavelength in microns. For convenience, Eq. (2) has been normalized relative to CO_2 laser wavelength (10.6μ) and to the fundamental properties of aluminum vapor $(A = 27$ and $T_v = 2750K$ at 1 atm pressure).

The vapor will remain in LTE when the laser flux is sufficiently low, $I \leq I_c$; nonequilibrium effects become dominant at higher fluxes $I \gg > I_c$.

A similar comparison of the electron heating time with the interelectron collision time shows that the free electrons can be characterized by a well-defined electron temperature unless the laser flux exceeds a value of about $10^9 (10.6/\lambda)^2$ w/cm². Similarly, translational equilibrium is maintained among the heavy particles (atoms and ions) at a well-defined heavy particle temperature, but the electron and heavy particle temperatures are significantly different unless the laser flux is sufficiently low, $I \leq I_c$.

As a consequence of the preceding results, avalanche ionization in the vapor can be analyzed on the basis of a "temperature" model in which the electrons are assumed to possess a Maxwell-Boltzmann energy distribution at a temperature different from the translational temperature of the heavy particles,[3] a model that is much simpler than the quantum-kinetic model required to treat the laser-induced breakdown of cold gases.[1,2]

Analysis of the appropriate kinetic rates indicates that nonequilibrium effects similar to those described can alter the internal structure of a laser-supported detonation (LSD) wave propagating through air at supersonic speed.[3] However, a similar analysis of a slow heating wave such as a subsonic laser-supported combustion (LSC) wave in air,[5] indicates that nonequilibrium phenomena are of minor significance over the range of laser intensities for which these waves have been observed experimentally.[6] The efficient coupling between free electrons and the vibrational states of air molecules makes nonequilibrium conditions harder to achieve than in an atomic gas.

III.   Theoretical Analysis and Comparison with Experiment

The simple interaction model described in Sec. I implies that the initiation of a laser-absorption wave in the air over a target is dependent on the large-scale evolution of vapor and the subsequent heating of the vapor by absorption of laser energy. Rough estimates of the time scales of those processes have been found to be consistent with the time scale of events observed experimentally with metal targets irradiated by a CO_2 gas laser at intensities up to a few Mw/cm² for 1 millisec or longer. This is the intensity range where subsonic LSC waves have been observed,[6] and where nonequilibrium phenomena are expected to play a minor role in the wave formation process.

A numerical solution to the laser-target interaction problem has been developed and implemented in a computer program called GLIT (Gasdynamics over Laser-Irradiated Targets). The program solves in an Eulerian coordinate system the one-dimensional, time-dependent equations that govern the gasdynamics, laser radiation transport, and spectral thermal radiation transport in the vapor and air layers; and accounts for heat conduction in the target and for surface vaporization. The basic equations and numerical solution technique are outlined in the Appendix.

Calculations have been performed for comparison with experimental data[6] in which subsonic LSC waves have been observed over titanium-alloy targets of 16-32-mil thickness irradiated by a CO_2 gasdynamic laser at peak intensities of the order of 0.1-1Mw/cm², pulse durations of 1-5 msec, and

Table 1   Experimental parameters[6]

Shot no.	Target thickness (mils)	Spot diameter (cm)	t_f (msec)
10	32	1.0	1.805
11	16	1.0	1.0
12	16	0.5	0.57

irradiated spot diameters of 0.5-1.3 cm. Of the dozen experimental shots for which a consistent set of data is available, three that were conducted in air at 1-atm pressure have been selected for detailed analysis. The basic experimental parameters are listed in Table 1. The last column in the table gives the experimentally measured time t_f after the beginning of the laser pulse at which the absorption wave was observed to form and begin propagating up the beam. A piecewise-linear curve-fit that accurately represents the measured laser intensity incident on the target in each shot[6,7] is plotted in Fig. 2.

Theoretical GLIT calculations were performed for each of the shots listed in Table 1, using the laser pulse histories of Fig. 2. An estimate of the sound-wave transit time in the vapor indicates that lateral expansion of the vapor will develop in a time scale of the order of a few microseconds, which is short compared to the millisecond time scale spanned by the theoretical calculations. To simulate lateral expansion effects, spherical geometry [$\omega = 2$ in Eqs. (6) and (7), Appendix] was employed with the target diameter equal to that of the measured laser spot. The one exception is that the laser radiation transport was approximated as planar [$\omega = 0$ only in the *laser* flux divergence term of Eq. (6d), Appendix] to simulate the weakly focused experimental beam. The beam convergence half-angle of 4.5° introduces only a minor variation in incident flux over the dimensions of the vapor and shocked air layers. It is easily verified that both the target thicknesses and irradiated spot radii of the experiments are large compared to the depth a thermal wave can penetrate into the material in the time t_f. This justifies the assumption of one-dimensional heat conduction that is employed in the analysis (see Appendix), and that will be made use of later to correlate the experimental data.

The interested reader is referred to Ref. 8 for a detailed description of the equations of state, radiation absorption coefficients, and target material properties that were employed in the computer calculations to be presented.

The predicted sequence of events for a typical shot (No. 12) is as follows: the only process that takes place prior to the onset of surface vaporization is laser energy absorption, and heat conduction in the target because the cold air is completely transparent to the incident laser beam. The surface reaches its vaporization temperature at $t_v = 0.4$ msec and begins to vaporize. A shock wave quickly forms in the air because of the piston effect of the expanding vapor. The time of shock formation is:[9] $t = t_v + 2c_\infty / (\gamma_\infty + 1)\dot{u}_0$, where γ_∞ is the specific heat ratio and c_∞ is the speed of sound in the ambient air, and $\dot{u}_0$ denotes the initial acceleration of the vapor piston. The GLIT code calculations were started near the time of shock formation, but before significant absorption of laser
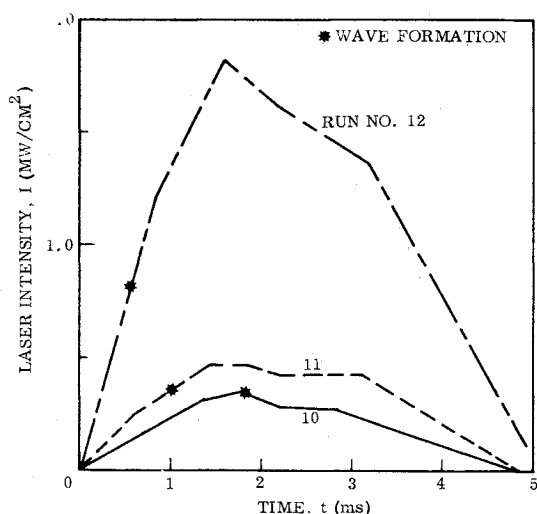
energy occurs in the vapor. The initial conditions were obtained from a self-similar solution for adiabatic flow.[4]

Figure 3 shows the computed temperature distributions in the gas layers at successive times after the start of the calculation. The abcissa X in this plot is defined in Eq. (15) of the Appendix. In Fig. 3, the air shock is so weak that the air temperature behind the shock is only slightly above ambient, far too low to cause air to absorb laser energy directly. However, the vapor is sufficiently ionized to absorb laser energy. A heating wave propagates inward toward the target surface as more and more energy is absorbed by the vapor. Some heating is also evident in the shocked air adjacent to the vapor layer, and an initially weak thermal wave advances into the shocked air. We shall see later that this initial heating of the air is due almost entirely to thermal radiation emitted by the hot vapor.

When the vapor reaches temperature near 20,000 K, it approaches a state of radiative equilibrium with the incident laser flux and cannot be heated further. Thermal radiation emitted by the hot vapor is absorbed in the adjacent air. Once the air reaches a temperature of about 8000K, the air is sufficiently ionized to begin absorbing laser radiation directly by inverse bremsstrahlung, and heating becomes very rapid. By the time the calculation was terminated at $t = 0.49$ msec, the air had reached a temperature of about 19,000K. At this time, only a fraction of the incident laser energy is transmitted to the vapor and an incipient laser absorption wave exists in the air. The temperature profiles are replotted in Fig. 4 as a function of the physical coordinate to display the growth of the vapor and air layers properly with time.

The thermal waves that are driven into the vapor toward the target and into the air toward the outer weak air shock are accompanied by strong pressure waves that rapidly evolve into shock waves. The computed pressure distributions are displayed in Fig. 5. The first inward-moving shock strikes the surface at about 0.48 msec and induces a momentarily high reflected shock pressure of about 17 atm. The reflected shock rapidly overtakes the embedded air shock that was formed initially by heating of the vapor. The strength of the resulting embedded shock is substantial at 0.49 msec (its pressure ratio is about 8). The Rankine-Hugoniot equations for a shock of
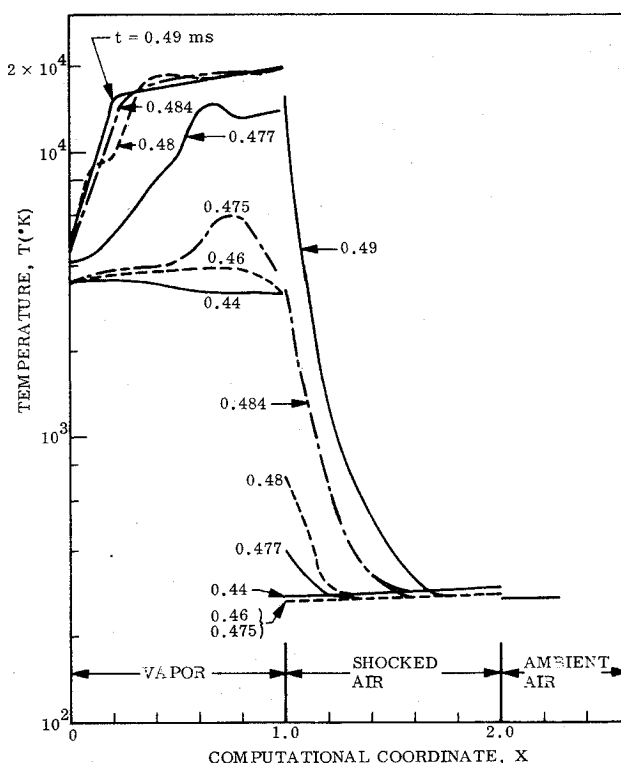

Fig. 2　Experimental laser intensity histories.[6,7]

Fig. 3　Temperature distributions at various times (run No. 12).
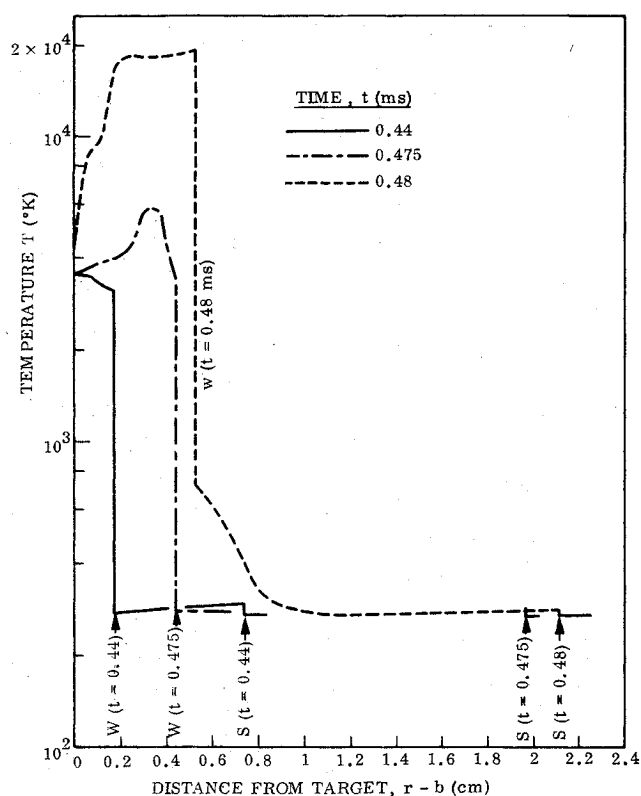
Fig. 4 Temperature distributions in physical space at various times (run No. 12).
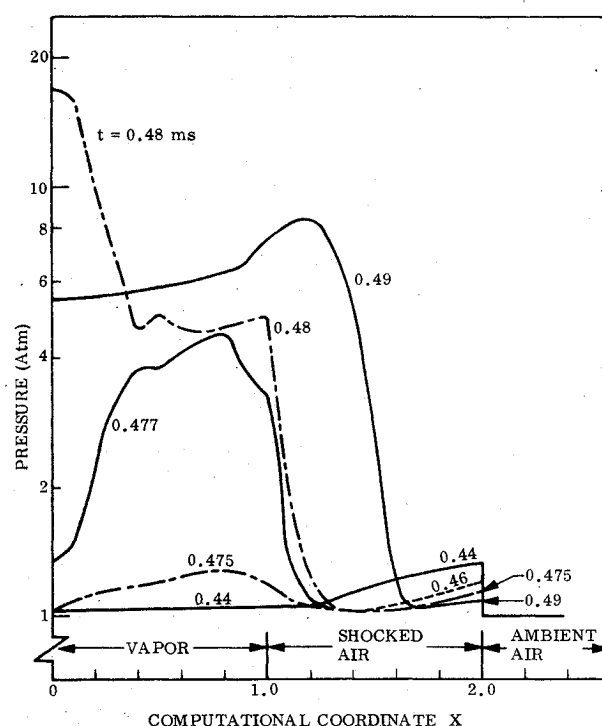

Fig. 5 Pressure distributions at various times (run No. 12).

Fig. 6 Spectral thermal radiation flux emitted by vapor and incident on shocked air (run No. 12).

this strength yield a peak shock temperature of only 700K; the electron density at this temperature is far too low to induce laser energy absorption by the air. This fact leads us to conclude that the incident absorption wave that has formed in the air is an LSC wave.

It is well known that an established absorption wave propagating through a cold gas is driven by the absorption of laser energy in the hot, ionized tail of the wave. Propagation of the wave hinges on the existence of a mechanism for heating the cold gas ahead of the wave to a temperature where the gas is sufficiently ionized to absorb laser energy. In an LSD wave, which moves at supersonic speed, the preheating is accomplished by a strong shock at the head of the wave whereas in the subsonic LSC wave the preheating is due to energy transported forward from the hot gas behind the wave, e.g., by thermal radiation transport.

Although both thermal radiation and shock preheating are present in the GLIT calculation, we have shown that the embedded air shock is too weak to support an LSD wave. This was confirmed by a similar GLIT calculation in which the thermal radiation absorption coefficients of the air were artificially set to zero. The air never reached a temperature in excess of 1000K before the end of the laser pulse and no absorption wave was formed.

Figure 6 shows the history of the thermal radiation flux emitted by the vapor toward the air in several spectral bands, along with the total flux. Over half of the total lies in the 7-11-ev band that is strongly absorbed by air in the Schumann-Runge system of the O_2 molecule. This radiant energy rapidly heats the air to temperatures of 4000-5000K at which the O_2 is largely dissociated. The high-frequency radiation above the
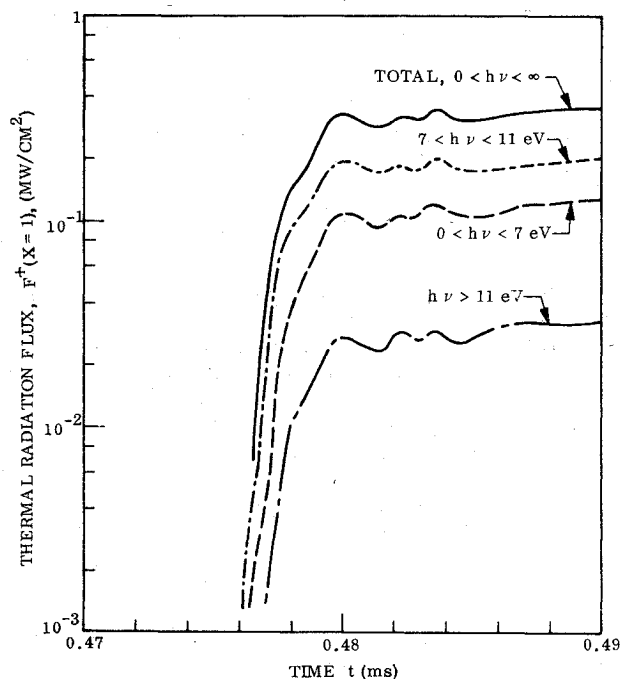
11-ev photoionization threshold of the air causes further heating to temperatures of 8000-10,000K, where sufficient electrons are liberated by thermal ionization for the air to absorb laser energy directly by the inverse bremsstrahlung mechanism that is responsible for initial heating of the vapor.

The theoretical results for Runs 10-12 are summarized in Table 2. The table includes the time t_v at which the surface first reaches its vaporization temperature; and the time t_f at which an incipient absorption wave exists in the air outside the vapor layer, as determined by the fact that the air has achieved a temperature of 20,000K and is absorbing most of the incident laser energy.

The computed wave formation times are seen to agree within 20% or better with those observed experimentally

Table 2 Theoretical results

Run no.	t_v(msec)	t_f(msec)
10	1.46	1.8
11	1.01	1.2
12	0.40	0.49

(Table 1). The close agreement tends to support the validity of the uniform surface vaporization model and of the physics of the wave formation process that were outlined at the beginning of the paper.

The theoretical results show that, under the conditions of these experiments, the bulk of time delay between the beginning of the laser pulse and the formation of an absorption wave consists of the time required to produce vapor. This part of the time delay is governed by surface absorption and heat conduction in the target. Laser heating of the vapor and subsequent heating of the air by thermal emission from the vapor occur relatively quickly. If this behavior were true of all the experimental shots, then one would expect the observed wave formation times to correlate as a function of the fundamental parameters that affect the heat conduction process. We shall show that this is the case.

During the period when the target is being heated up to its vaporization temperature, the surface temperature history is governed by the following exact solution to the equation of one-dimensional heat conduction.[10]

$$T - T_b = [(1-R) / (\pi k \rho C)^{1/2}] \int_0^t (t-t')^{-1/2} I(t') dt' \quad (3)$$

where I is the laser intensity, R the target surface reflectivity; and k, ρ, C, and T_b are the target material conductivity, density, heat capacity, and initial bulk temperature, respectively. Upon performing an integration by parts, we obtain the following equation for the time of onset of vaporization

$$t_v = \{ (9\pi/16) k\rho C [(T_v - T_b)/(1-R)]^2 \}^{1/3} <\dot{I}>^{-2/3} \quad (4)$$

where

$$<\dot{I}> = \frac{3}{2} \int_0^1 (1-\xi)^{1/2} \dot{I}(\xi) d\xi \qquad \xi = t/t_v \quad (5)$$

represents a weighted average of the laser pulse slope $\dot{I} = dI/dt$ up to the onset time. This average slope is the fundamental laser beam parameter that governs the time required to produce vapor. Thus, if the behavior predicted by the GLIT calculations were true of the cited experiments, then the observed times should correlate well as a function of the average slope of the laser pulse up to the formation time, as given by Eq. (5).

The correlation is displayed in Fig. 7, which contains all experimental points for which a self-consistent set of data is available,[7] including shots for ambient pressures other than 1 atm. For reference, Eq. (4) is plotted as the solid line in Fig. 7.

The correlation among experimental data points is reasonably good. Most striking is the fact that the data follow the trend predicted by Eq. (4), namely, that the wave formation time varies as $<\dot{I}>^{-2/3}$. This fact is very strong evidence of the fundamental validity of the uniform surface vaporization model and of the basic physics of the wave formation process that was described earlier. That is, the generation of a vapor layer is a necessary precondition to the formation of an absorption wave; inverse bremsstrahlung absorption of laser energy takes place in the initially weakly-ionized vapor; thermal radiation emitted by the hot vapor then heats the air to temperatures at which it is ionized sufficiently to absorb laser energy directly, and an absorption wave is formed.

Although the successful correlation displayed in Fig. 7 might tempt one to conclude that a simple scaling based upon the laser beam and target material parameters that govern the vaporization onset time is valid in general, the LSC wave formation phenomena also involve gasdynamic effects as well as wavelength-dependent absorption and emission processes that occur in the vapor and air. The only conclusion warranted is that the basic physical model and analysis presented here are fundamentally valid, and represent useful tools that can be
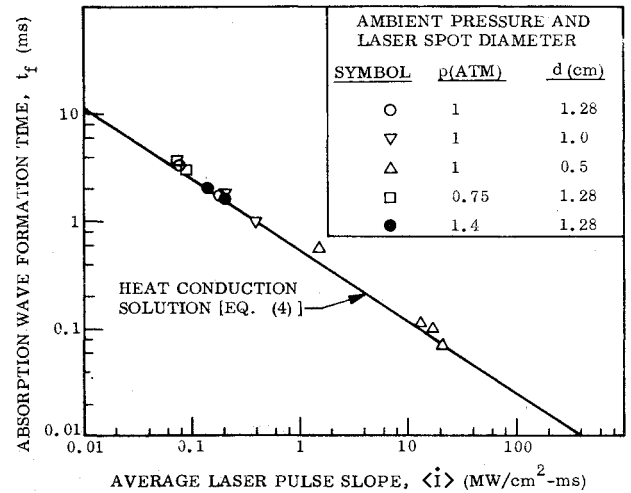

Fig. 7 Correlation of experimental data on LSC wave formation over titanium targets[6,7], $\lambda = 10.6\mu$.

used to investigate the laser-target interaction and LSC wave formation phenomena for laser beam and target material parameters other than those for which the foregoing numerical results have been obtained.

Appendix:

Basic Equations and Numerical Solution Technique

The GLIT computer program described in Sec. III performs a numerical solution of the laser-target interaction problem based upon the model illustrated in Fig. 1. The equations and techniques used to solve them numerically are presented herewith.

Equations

The flow in each of the three gas regions depicted in Fig. 1 is assumed to be one-dimensional and inviscid. The basic equations that express global conservation of mass, momentum, and energy with respect to an Eulerian frame of reference that is fixed relative to the solid target may be expressed in vector notation as follows

$$H_t + B_r + C_r + D = 0 \quad (6a)$$

$$H = r^\omega \rho (1, u, \epsilon)^T \quad (6b)$$

$$B = r^\omega (\rho u, p + \rho u^2, up + \rho u \epsilon)^T \quad (6c)$$

$$C = r^\omega (0, 0, Q + F)^T \quad (6d)$$

$$D = (0, \omega p r^{\omega-1}, 0)^T \quad (6e)$$

where (r, t) are the space and time variables, respectively; ρ, p, e, and $\epsilon = e + u^2/2$ represent the density, pressure, specific internal energy, and total energy, respectively; u is the particle velocity in the r-direction; Q and F are the laser and thermal radiation fluxes, respectively; and ω is a geometric index such that the equations are valid for planar, cylindrical, or spherical symmetry when $\omega = 0, 1, 2$, respectively.

For the thermal radiation transport, we employ Landshoff's generalization[11] of the Schuster-Schwarzschild "two-stream" approximation,[1] which leads to the following pair of equations for the spectral unidirectional flux F_v^+, F_v^- in the positive and negative r directions, respectively

$$r^\omega F_v^\pm \exp(\pm \tau_v) = \int r^\omega \pi B_v \exp(\pm \tau_v) d\tau_v + C^\pm \quad (7)$$

where B_v is the Planck function and τ represents the effective optical depth along the "average ray" whose direction cosine

relative to the r direction is $\ell = \frac{1}{2}$

$$\tau_\nu = 2 \int_b^r \kappa_\nu \, dr \tag{8}$$

κ_ν is the spectral absorption coefficient and $C^\pm$ are integration constants that are evaluated easily in terms of the known boundary conditions on $F_\nu^\pm$. The net spectral flux is given by

$$F_\nu = F_\nu^+ - F_\nu^- \tag{9}$$

which must be integrated over frequency to obtain the total flux F.

As long as the electron density everywhere is less than the critical density corresponding to the laser frequency, the incident and reflected laser beam intensities $I^\pm$ and net laser flux Q for an unfocused beam are given by Eqs. (7) and (9) if we substitute $\omega = B_\nu = 0$, $F_\nu^\pm \to I^\pm$, $F_\nu \to Q$, and omit the factor 2 from Eq. (8).

Boundary Conditions

The outer boundary conditions are

$$p \to p_\infty \quad \rho \to \rho_\infty \quad u \to 0 \quad I^- \to I_\infty^- \quad F_\nu^- \to 0 \text{ as } r \to \infty \tag{10}$$

The air shock is a free boundary surface at which the Rankine-Hugoniot jump conditions apply as boundary conditions.

The air-vapor contact surface is a tangential discontinuity across which the pressure p and particle velocity u must be continuous, but all other flow variables may be discontinuous.

Finally, if the target is not undergoing surface vaporization, then the appropriate boundary condition is

$$u = 0 \text{ at } r = b \tag{11}$$

If surface vaporization occurs, we require a boundary condition that specifies the vaporization rate as a function of the gasdynamic state of the vapor adjacent to the surface and of the total laser and thermal radiation flux incident on the surface. This relationship depends on the radiative transfer and heat conduction within the solid. We assume that the surface pressure is low compared to the critical pressure of the material (for most materials of interest, the latter is of the order of 10 kbar), so that there exists a zone near the instantaneous surface of the unvaporized material within which the material undergoes a transition from the condensed phase to the vapor phase. Following Vilenskaia and Nemchinov,[12] we shall refer to this zone as the "vaporization wave." The material at any point within this wave consists of a mixture of condensed and vapor phases. We shall restrict our attention to opaque materials for which the radiation absorption coefficient of the condensed phase is very large compared to that of the vapor phase. Then the vaporization wave is opaque and is thin compared to the vapor layer dimensions. The processes that occur within the wave then may be treated as quasi-steady in a coordinate system fixed on the instantaneous surface of the unvaporized material. The states of the material on either side of the wave are connected by jump conditions that express the conservation of mass, momentum, and energy. The vapor and solid densities satisfy the inequality $\rho_0 << \rho_b$, and jump equations may be written in the form

$$\dot{m} = -\rho_b \dot{b} = \rho_0 u_0 \tag{12a}$$

$$p_b = p_0 + \dot{m} u_0 \tag{12b}$$

$$\dot{m} L = q_0 - \lim_{r \to b^-} (k_b \partial T / \partial r) \tag{12c}$$

where $\dot{m}$ denotes the mass vaporization rate, $\dot{b}$ is the surface recession velocity, L is the latent heat of vaporization, k is the thermal conductivity, the subscripts 0 and b refer to conditions at the vapor and condensed-phase sides of the wave, respectively; and q_0 represents the net radiant flux per unit area absorbed within the wave.

Equation (12c) represents the boundary condition under which the heat conduction equation must be solved for the region within the vaporizing solid. By employing Goodman's approximate integral method,[13] the heat conduction problem can be reduced to the following ordinary differential equation, which is easily solved numerically:

$$(3/4) \ (d/dt) \ [\ (k\rho \, C)_b (T_0 - T_b)^2 / (q_0 - \dot{m} L) \ ]$$
$$= q_0 - \dot{m} \ [L + C_b (T_0 - T_b)] \tag{13}$$

where C_b is the heat capacity and T_b the initial bulk temperature of the solid.

Following Vilenskaia and Nemchinov,[12] we assume that local thermodynamic equilibrium including phase equilibrium, is established at a point near the vapor side of the vaporization wave. The temperature T_0 is then a unique function of the local pressure p_0 as given by the phase equilibrium relation, which may be accurately represented by a function of the form

$$T_0 / T_v = (1 - A \ln p_0)^{-1} \tag{14}$$

where p_0 is the pressure in atm, T_v is the normal boiling point, and A is a constant for any given material.

Coordinate Transformations

Equation (6) is to be solved numerically by forward integration in time, subject to the described boundary conditions. Because the shock and contact surface are free boundaries, the implementation of the numerical solution is greatly simplified if the three flow regions (vapor layer, shocked air layer, and external air layer) are first mapped onto a transformed space in which each region occupies an interval of fixed length.

Let the instantaneous positions of the target, contact surface, and shock surface be denoted by the equations $r = b(t)$, $r = w(t)$, and $r = s(t)$, respectively. We introduce a transformation from the physical coordinate r to the computational coordinate X defined by the following mapping function:

$$X = (r - b)/(w - b) \quad b \leq r \leq w \tag{15a}$$

$$= 1 + (r - w)/(s - w) \quad w \leq r \leq s \tag{15b}$$

$$= 2 + \tanh \ [\beta(r - s)] \quad r \geq s \tag{15c}$$

where β is an arbitrary stretching coefficient.

The coordinate transformation maps the target surface, contact surface, and shock onto the fixed points $X = 0$, $X = 1$, and $X = 2$, respectively. The point at infinity is mapped onto the point $X = 3$. Equation (6) may be expressed in conservation-law form with respect to the transformed coordinate. The result is

$$A_t = -(E_X + C_X + G) \tag{16a}$$

where

$$A = r_X H \quad G = r_X D \tag{16b}$$

$$E = r^\omega [\rho(u - r_t), p + \rho u(u - r_t), up + \rho \epsilon (u - r_t)]^T \tag{16c}$$

$$r_X = 1/X_r \quad r_t = -X_t / X_r \tag{16d}$$

To complete the formulation, we require a set of equations that govern the motion of the target surface, contact surface, and shock, and that govern the flow at the corresponding boundary surfaces.

The flow at the boundary surfaces is treated by a method similar to that used in Ref. (14) for computing steady, supersonic flows. The flow variables on either side of the shock are related by the well-known Rankine-Hugoniot equations expressing mass, momentum, and energy conservation. The latter equation may be written in terms of effective specific heat ratios γ_3 and γ_2 before and behind the shock, respectively, where γ is defined by the equation

$$\gamma = 1 + (p/\rho e) \qquad (17)$$

and where the subscripts 2, 3 refer to the shocked air and external air regions, respectively. The shock equations then may be solved explicitly as functions of the parameters γ_2, γ_3, and the shock pressure ratio $\xi = p_2/p_3$. This procedure yields the following expressions for the shock speed $\dot{s}$ and for the flow variables behind the shock

$$\dot{s} = u_3 + \left\{ \frac{(\gamma_2 + 1)p_3}{2\rho_3} \right.$$
$$\left. \left[\xi + \left(\frac{\gamma_2 - 1}{\gamma_2 + 1} \right) \right] / \left[1 + (\gamma_3 - \gamma_2)/(\gamma_3 - 1)(\xi - 1) \right] \right\}^{1/2}$$
$$\qquad (18a)$$

$$u_2 = u_3 + \frac{2(\dot{s} - u_3)}{\gamma_2 - 1}$$
$$\left[\xi - \left(\frac{\gamma_2 - 1}{\gamma_3 - 1} \right) \right] / \left[\left(\frac{\gamma_2 + 1}{\gamma_2 - 1} \right) \xi + 1 \right] \qquad (18b)$$

$$\frac{\rho_2}{\rho_3} = \left[1 + \xi \left(\frac{\gamma_2 + 1}{\gamma_2 - 1} \right) \right] / \left[\xi + \left(\frac{\gamma_3 + 1}{\gamma_3 - 1} \right) \right] \qquad (18c)$$

These last equations, taken together with the equation of state $e = e(p, \rho)$ are sufficient to determine the values of the flow variables immediately behind the shock (region 2) in terms of the values in region 3 at the upstream side of the shock if the shock pressure p_2 is known from solving the limiting form of Eq. (16) at the downstream side of the shock. The use of the parameter γ defined by Eq. (17) involves no approximation, but is valid for any gas in LTE.[14]

Equation (18a) is a total differential equation that can be integrated numerically along with Eq. (16) to determine the shock trajectory. The left-hand equality in Eq. (12a) represents a similar differential equation for the motion of the target surface. Similarly, the air-vapor contact surface moves with the fluid velocity

$$\dot{w} = u(X = 1, t) \qquad (19)$$

Numerical Solution

Computational Mesh

The described equations are solved by forward integration in time. Each of the three flow regions is subdivided into a uniform mesh in the X direction. The mesh points are arranged so that one mesh point lies at the target surface $X = 0$ and one at the outer boundary $X = 3$; whereas each of the two internal boundary surfaces $X = 1, 2$ is covered by two mesh points because the flow variables may be discontinuous at these surfaces.

Difference Equations

Let the solution to Eq. (16) be known at the nth time level t^n for each mesh point j. The solution at the next time level t^{n+1}

$= t^n + \Delta t$ is obtained by using an explicit two-step predictor-corrector sequence of the form

$$\text{Predictor: } \tilde{A}_j^{n+1} = A_j^n + \Delta t (A_t)_j^n \qquad (20a)$$

$$\text{Corrector: } A_j^{n+1} = (\frac{1}{2})[A_j^n + \tilde{A}_j^{n+1} + \Delta t (\tilde{A}_t)_j^{n+1}] \qquad (20b)$$

At points interior to any of the flow regions, the terms that comprise A_t (i.e., the terms of the right-hand side of Eq. (16a) are evaluated numerically as follows: for the gasdynamic term E_X, we use the scheme originated by MacCormack,[15] which employs forward differences in the predictor and backward differences in the corrector. The term C_X that involves the radiative fluxes is evaluated from a central difference formula in both predictor and corrector.

The described difference equations are of uniform second-order accuracy in both space and time increments ΔX, Δt. They have been used successfully to compute flows with embedded shocks,[16] and their numerical stability properties have been established for nonradiating flows.[15] The radiative transport terms necessitate additional stability criteria,[5] which are too lengthy to be included here.

The boundary $X = 3$ is the image in the computational space of the point $r = \infty$, and the flow variables are held fixed at the values given in Eq. (10). The flow at the other boundaries is computed from the governing equations by employing first-order one-sided difference formulas in which the differences are taken in the same direction for both predictor and corrector.[14] The shock location at the advanced time t^{n+1} is computed by applying to Eq. (18a) a predictor-corrector formula similar to Eqs. (20). Once the flow variables on both sides of the shock are computed from Eqs. (20), the shock jump conditions are imposed as follows: the computed values of all flow variables upstream of the shock, together with the computed pressure on the downstream side are used in Eqs. (18b,c) to re-evaluate the remaining flow variables at the downstream side. This procedure is followed upon completing either the predictor or the corrector step of Eq. (20) for all mesh points. In the case of weak shocks ($\xi \approx 1$) improved accuracy is obtained if Eqs. (18) are recast in terms of the computed particle velocity u_2 rather than ξ.

If ($\dot{m} > 0$), then a similar procedure is used to satisfy the surface boundary conditions —Eqs. (12)-(14)—in terms of the computed surface pressure and radiation flux, provided the resulting vapor velocity at the surface is subsonic. If a supersonic velocity results, the Eqs. (12) and (14), together with the sonic-flow Jouget condition $u_0 = c_0$ and the vapor equation of state, form a closed system of equations from which the surface flow variables are computed directly. When $\dot{m} = 0$, a special technique is used to satisfy the proper surface boundary condition, Eq. (11). The technique is similar to the one described following that is employed at the contact surface.

Both pressure and particle velocity must be continuous across the contact surface. We use the limiting form of Eq. (16) to compute the flow variables at either side of the discontinuity. Because of the inevitable error inherent in the numerical integration procedure, the computed results will not satisfy precisely the stated boundary conditions. To eliminate the erroneous discontinuity in pressure and particle velocity, we make use of a technique similar to the "simple wave corrector" technique originated by Abbett[17] for satisfying the exact boundary condition at an impermeable surface in steady, supersonic flow. The essence of the method is to employ a fundamental solution of the gasdynamic equations to equalize the pressure and particle velocity on the two sides of the contact surface. The required fundamental solution is the well-known, self-similar solution for the flow resulting from discontinuous initial conditions and is discussed thoroughly in Landau and Lifschitz.[9]

References

[1] Zel'dovich, Ya. B. and Raizer, Y. P., *Physics of Shock Waves and High-Temperature Hydrodynamic Phenomena*, Vol. 1, Academic Press, New York, 1966.

[2]Canavan, G. H., Proctor, W. A., Nielsen, P. E., and Rockwood, S. D., "CO_2 Laser Air Breakdown Calculations," Digest of Technical Papers, VII *International Quqntum Electronics Conference*, Montreal, Can., May 8-11, 1972.

[3]Thomas, P. D. and Musal, H. M., "Theoretical Study of Laser-Target Interaction," First Semi-annual Technical Report, LM-SC/D313142, Dec. 22, 1972, Lockheed Palo Alto Research Lab., Palo Alto, Calif.

[4]Thomas, P. D., "Estimates of the Early-Time Gasdynamics of Laser Beam-Target Interaction," LMSC/D267440, Lockheed Palo Alto Research Lab., Palo Alto, Calif., June 1, 1972.

[5]Thomas, P. D. and Musal, H. M., "Theoretical Study of Laser-Target Interaction," Final Technical Report, LMSC/D352890, Aug. 31, 1973, Lockheed Palo Alto Research Lab., Palo Alto, Calif.

[6]Klosterman, E. L. and Byron, S. R., "Experimental Study of Subsonic Laser-Absorption Waves," AFWL-TR-74-003, Dec. 1973, Mathematical Sciences NW, Inc., Seattle, Wash.

[7]Klosterman, E.L., private communication, Seattle, Wash., March 1974.

[8]Thomas, P. D., "Laser Absorption-Wave Formation," AIAA Paper 74-566, Palo Alto, Calif., June, 1974.

[9]Landau, L. D. and Lifschitz, E. M., *Fluid Mechanics*, Addition-Wesley, Reading, Mass., 1959.

[10]Ready, J. F., *Effects of High Power Laser Radiation*, Academic Press, New York, 1971, p. 73.

[11]*Thermal Radiation Phenomena*, Vol. 5, "Radiation Hydrodynamics of High-Temperature Air," DASA 1917-5, R. K. M. Landshoff, ed., Lockheed Missiles & Space Co., Sunnyvale, Calif., Nov. 1967.

[12]Vilenskaia, G. G. and Nemchinov, I. V., "Numerical Analysis of the Motion and Heating, by Laser Radiation, of a Plasma Being Formed in an Absorption Flare in the Vapors of a Solid," *Prikladnaia Mekhaniki i Tekhnicheskoi Fiziki,* No. 6, 1969, pp. 3-19.

[13]Goodman, T. R., "Heat Balance Integral and Its Application to Problems Involving a Change of Phase," 1957 Heat Transfer and Fluid Mechanics Institute, Stanford Univ. Press, Stanford, Calif., 1957.

[14]Thomas, P. D., Vinokur, M., Bastianon, R. A., and Conti, R. J., "Numerical Solution for Three-Dimensional Inviscid Supersonic Flow," *AIAA Journal*, Vol. 10, July 1972, pp. 887-894.

[15]MacCormack, R. W., "Effects of Viscosity in Hypervelocity Impact Cratering," AIAA Paper 69-354, Cincinnati, Ohio, 1969.

[16]Kutler, P., "Applications of Selected Finite-Difference Techniques to Solution of Conical-Flow Problems," Ph.D. thesis, Oct. 1969, Iowa State Univ., Ames, Iowa.

[17]Abbett, M. J., "Boundary Condition Calculation Procedures for Inviscid Supersonic Flowfields," *Proceedings, AIAA Computational Fluid Dynamics Conference*, Palm Springs, Calif., July 19-20, 1973.